Supplementary Information

Realizing a high-performance n-type thermogalvanic cell by tailoring thermodynamic equilibrium

Sungryong Kim[a], Jin Han Kwon[b], Yurim Bae[a], Jeongsu Kim[a], Taiho Park[a*], and Hong Chul Moon[b*]

Contents

Figure S17. The complex capacitance of the PLAMHQ1.0 under a) 50% RH, b) 70% RH, and c) 90% RH at frequencies 10^0 and 10^6 Hz at DC voltages of 0, 0.25, and 0.50 V.

Figure S18. The observed changes in pH according to the water retention in the polymer matrix at various RH conditions (50%, 70%, and 90% RH) and 70 ^oC.

Figure S19. Bode plots of PLAMHQ1.0 at various RH conditions (50%, 70%, and 90% RH).

Figure S20. The initial ΔV *vs.* time profiles of PLAMHQ1.0 at a) 50% RH, b) 70% RH, and c) 90% RH. The ΔV *vs.* time profiles of PLAMHQ1.0 at d) 50% RH, e) 70% RH, and f) 90% RH.

Figure S21. a, b, and c) The ΔV *vs.* time profiles of the completely dried PLAMHQ1.0 depending on the temperature difference (ΔT) and after removing the temperature gradient.

Figure S22. Photographic images showing the solution color of a) the PLSPHQ1.0, b) the PLAMHQ0.5, and c) the PLAMHQ1.0.

Figure S23. The ΔV *vs.* ∆T plots of the PLSPHQ1.0.

Figure S24. The voltage and thermopower of the PLAMHQ1.0 at ∆T = 5 K after various amounts of self-healing time.

Figure S25. The voltage *vs*. time profiles of the PLAMHQ1.0 under 0, 100, 200, and 300% uniaxial stretching at ∆T = 5 K.

Figure S26. a) voltage depending on the number of cycles and b) ΔV *vs.* time profiles at ΔT = 5 K.

Table S1. Performance calculation values for each performance of PLAMHQ0.5 and PLAMHQ1.0.

Table S2. A comparison of the TGC performance, thermopower, Carnot relative efficiency, stretchability, and self-healing capability of previously-reported TGC devices.

Supplemental references

Note 1. Redox reaction and reduction potential relation.

In general, it is challenging to maintain a standard state. Therefore, assuming a non-standard state, the relationship between the Gibbs free energy (ΔG) and the PCET reaction is defined as Eq. (N1):

$$\Delta G = \Delta G^{\circ} + RTln(\frac{[HQ]}{[BQ][H^+]^2}) \quad \text{(N1)}$$

where ΔG°, R, T, and [x] are the Gibbs free energy in the standard state, the ideal gas constant, the absolute temperature, and the species concentration, respectively. Moreover, the Gibbs free energy is related to the reduction potential (E) according to Eq. (N2):

$$\Delta G = -nFE \quad \text{(N2)}$$

where n and F are the number of electrons involved in the reaction and the Faraday constant, respectively.

Combining Eqs. (N1) and (N2) give an expression for the reduction potential (E) as Eq. (N3):

$$E = -\frac{\Delta G^{\circ}}{nF} - \frac{RT}{nF}\ln\left(\frac{[HQ]}{[BQ][H^+]^2}\right) = E^{\circ} - \frac{RT}{nF}\ln\left(\frac{[HQ]}{[BQ][H^+]^2}\right) \quad \text{(N3)}$$

where E° is the reduction potential in the standard state. Thus, α of the TGC based on PCET reaction is represented as Eq. (N4):

$$\alpha = \frac{\Delta E}{\Delta T} = \frac{-\frac{R}{nF}(T_H \ln\left(\frac{[HQ]_H}{[BQ]_H[H^+]_H^2}\right) - T_C \ln\left(\frac{[HQ]_C}{[BQ]_C[H^+]_C^2}\right))}{T_H - T_C} \quad \text{(N4)}$$

where H and C are the hot side and cold side, respectively. Since the H^+ migration is impeded by anionic polymer (AP), and assuming that H^+ on both the hot and cold sides are the same, it is expressed as follows Eq. (N5):

$$\alpha = \frac{\Delta E}{\Delta T} = \frac{-\frac{R}{nF}(T_H \ln\left(\frac{[HQ]_H}{[BQ]_H}\right) - T_C \ln\left(\frac{[HQ]_C}{[BQ]_C}\right))}{T_H - T_C} + \frac{R}{nF}\ln([H^+]^2) \quad \text{(N5)}$$

Eq. (N5) indicates that an increase in the concentration of the specific material contributes to genera ting more electricity. Thus, the extent of the PCET reaction is directly correlated with α, which is strong ly affected by the concentration of species in the reaction. In particular, to achieve high α of the TGC a s n-type system, $[HQ]_C$ should be maximized and the presence of minimal $[H^+]$ and $[BQ]_C$ is necessary near the cold electrode. For this purpose, we carefully designed the PLAM to include 2-acrylamido-2-methyl-1-propane sulfonic acid (AMPS) and lithium 3-sulfopropyl methacrylate (LSP). In specific, AMP S provided additional H^+ and remained low pH over the entire polymer matrix. Thus, overall [HQ] in the polymer matrix was maximized in accordance with Le Chatelier's principle (i.e., the reverse PCET reac tion) (**Fig. S11**). The anionic sites of LSP selectively captured H^+, preventing its migration to the cold e lectrode via the Soret effect (**Fig. 1d**, **1e**, **3d**, **3e**, **S3**, and **S12**). Additionally, AMPS supported the capt uring of H^+. As a result, a high concentration of HQ could selectively accumulate near the cold electrod e. These contributions are concluded as the origin of the outstanding performance, including high ther mopower, of the n-type TGC in this work.

Note 2. The calculation of the complex capacitance depending on the frequency.

To calculate the complex capacitance ($C(w)$) depending on the frequency, the real ($Z'(w)$) and imaginary ($Z"(w)$) impedance were measured through the electrochemical impedance spectroscopy (EIS). The impedance ($Z(w)$) was expressed by Eq. (N6):

$$Z(w) = Z'(w) + jZ"(w) \quad \text{(N6)}$$

where the j is the imaginary number. The relation between $Z(w)$ and $C(w)$ is as follows Eq. (N7):

$$Z(w) = \frac{1}{jwC(w)} \quad \text{(N7)}$$

Therefore, real ($C'(w)$) and imaginary ($C"(w)$) capacitance are defined Eqs. (N8) and (N9)

$$C'(w) = \frac{-Z"(w)}{w|Z(w)|^2} \quad \text{(N8)}$$

$$C"(w) = \frac{Z'(w)}{w|Z(w)|^2} \quad \text{(N9)}$$

As a result, $C(w)$ profile ($C(w) = C'(w) - jC"(w)$) was extracted from the real and imaginary part.[S1] In this study, the EDL region is determined based on the region where real & imaginary capacitance are equal (~ 10^3 Hz).[S2]

Note 3. The synthesis of the polymers.

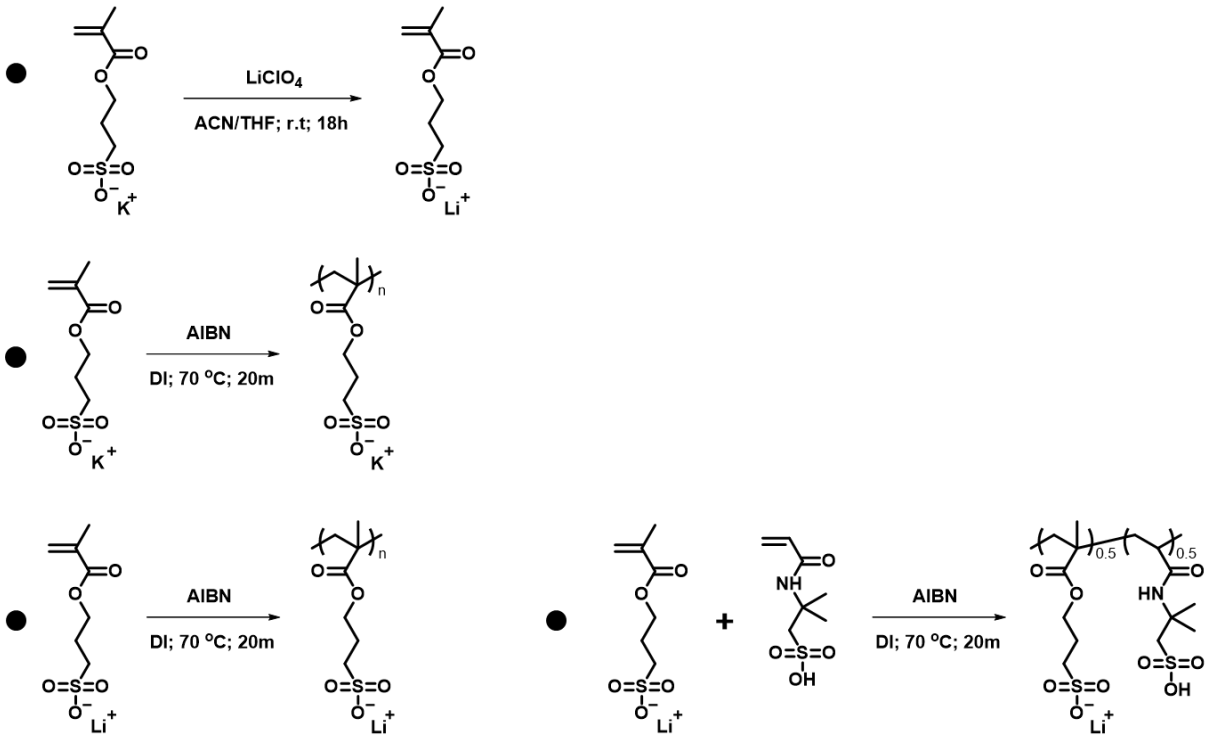

Synthesis scheme for Li[SPMA], PKSP, PLSP, and PLAM polymers

Materials

3-Sulfopropyl methacrylate potassium salt, Lithium perchlorate, 2, 2'-azobis(isobutyronitrile), and 2-acrylamido-2-methyl-1-propanesulfonic acid were purchased from the Sigma-Aldrich.

Synthesize of 3-sulfopropyl methacrylate lithium salt (Li[SPMA]).

3-Sulfopropyl methacrylate potassium salt (11.07 g, 45 mmol) and Lithium perchlorate (5.75 g, 54 mmol) were mixed in 30mL tetrahydrofuran/acetonitrile co-solvent ((5/5), v/) for ion exchange (at room temperature, 12 h). The solution was centrifuged (5000rpm, 5min). After that, the solvent of the supernatant was removed by a rotary evaporator. The product was dried in a vacuum oven for 10^{-3} torr (over 24 h). The yield was 89.4% (8.62 g, 40 mmol). ^{1}H-NMR (500 MHz, D2O, δ): 6.14 (s, -CH), 5.71 (s, -CH), 4.28 (t, *J* = 6.3, -CH2), 3.02 (t, *J* = 7.3, -CH2), 2.14 (m, *J* = 7.4, -CH2), 1.92 (s, -CH3). ^{7}Li-NMR (500MHz, D2O, δ): 0.12 (s, -Li^{+}). ^{13}C-NMR (500MHz, D2O, δ): 169.79, 135.92, 126, 63.76, 47.81, 23.72, 17.40

Synthesize of PKSP.

3-Sulfopropyl methacrylate potassium salt (12.10 g, 50 mmol) and 2, 2'-azobis(isobutyronitrile) (0.012 g, 0.75 mmol) were used for polymerization in water (at 70 ℃, 24 h). Three precipitations were

proceeded in methyl alcohol. The product was dried in a vacuum oven for 10^{-3} torr (over 24 h). The final white solid product was obtained (6.32 g). ^{1}H NMR (500 MHz, D2O, δ): 4.58-3.68 (br, -CH2), 3.04-2.94 (br, -CH3), 2.30-1.48 (br, -CH2, -CH2), 1.36-0.63 (br, -CH3).

Synthesize of PLSP.

3-Sulfopropyl methacrylate lithium salt (10.86 g, 50 mmol) and 2,2'-azobis(isobutyronitrile) (0.012 g, 0.75 mmol) were used for polymerization in water (at 70 ℃, 24hour). Three precipitations were proceeded in tetrahydrofuran. The product was dried in a vacuum oven for 10^{-3} torr (over 24 h). The final white solid product was obtained (5.16 g). ^{1}H NMR (500 MHz, D2O, δ): 4.30-3.84 (Br, -CH2), 3.01-2.91 (Br, -CH2), 2.18-1.49 (Br, -CH2, -CH2), 1.29-0.71 (Br, -CH3).

Synthesize of PLAM.

3-Sulfopropyl methacrylate lithium salt (5.43 g, 25 mmol), 2-acrylamido-2-methyl-1-propanesulfonic acid (5.18 g, 25 mmol), and 2, 2'-azobis(isobutyronitrile) (0.012 g, 0.75 mmol) were used for polymerization in water (at 70 ℃, 24hour). Three precipitations were proceeded in tetrahydrofuran. The product was dried in a vacuum oven for 10^{-3} torr (over 24 h). The final white solid product was obtained (4.79 g). ^{1}H NMR (500 MHz, D2O, δ): 4.49-3.90 (Br, -CH2), 3.45-3.03 (Br, -CH2, -CH2), 2.36-1.95 (Br, -CH2, -CH2, -CH2), 1.64-0.90 (Br, -CH3, -CH, -CH3).

Preparation of the hydrogels

The polymers (1 g) were dissolved in the 5wt% glycerol aqueous (10 g) (0.5 g glycerol/9.5 g DI water). In PLAMHQ0.5 and PLAMHQ1.0, HQ was dissolved in the solution. The solution was drop cast on the Teflon mold. After that, the solution dried at 60 ^{o}C for 5 h.

Characterization of the polymers

^{1}H, ^{7}Li, and ^{13}C NMR spectroscopy were measured on an Avance III HD500 instrument using deuterium oxide. The electrochemical properties of the hydrogels were measured using electrochemical impedance spectroscopy (EIS; IM6, Zahner). The resistance of the hydrogels was measured by the high-frequency intercept of the semi-circle in the Nyquist plot with sandwiched devices of FTO glass. The resistivity (ρ) of the ionic conductor was calculated as following:

$$\rho = RA/l \quad (4)$$

where R is the resistance, A is the area, and l is the thickness of the hydrogel. The rheological properties were obtained using an MCR-92, Anton Paar Rheometer with an 8 mm parallel plate on an oscillation basis, and the absorbance spectra were measured with a Mecasys Optizen Pop UV/Vis

spectrophotometer. Differential scanning calorimetric (DSC) measurements were performed using a Perkin-Elmer Pyris DSC 4000 instrument under an N_2 atmosphere at a heating and cooling rate of 10 °C/min. A tensile test was performed using ESM303, Mark-10 with the specimen of cylindrical shape with a diameter of 2 mm and length of 2 cm (tensile speed of 100 mm min^{-1}). The optical microscopy images were obtained using an optical microscope (ZEISS Axioplan microscope). The thermoelectric properties were measured using the source measure unit (SMU, Keithley 2400) and 2 Peltier devices to establish a temperature gradient. The stabilization process continued until the potential difference between the electrodes reached 0.3 mV or below. Subsequently, a temperature gradient was applied. Current density was measured through the voltage sweep method using the sandwich structure TGC after sufficient thermo-voltage was formed by the temperature gradient. The thermal conductivity was determined by the laser flash analysis (LFA) method. To light up the LED, wearable TGC was aided by a voltage amplifier (AD620).

Device fabrication and measurement

Rigid TGC.

Silver paste as the electrode was stacked on bare glass (1 × 5 cm^2). The glass was annealed on the 50 ^oC hot plate for 2 h. The VHB 4905 with (1 × 3 cm^2) hole was stacked on the bare glass and silver paste electrodes. The solution was drop cast on the bare glass and silver paste electrode (1 × 3 cm^2). The DI water dried at 60 ^oC for 5 h. The voltage of the thermogalvanic cells was measured using the Keithley 2450 source meter. The temperature gradient was applied from the 2 Peltier devices.

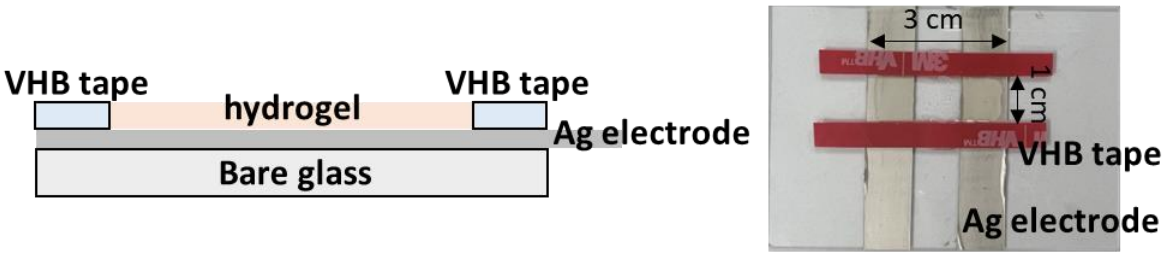

Stretchable TGC.

Copper tapes were stacked on the VHB tape (1 × 5 cm^2). The VHB tape with (1 × 3 cm^2) hole was stacked on the VHB tape and Copper electrodes. The solution was drop cast on the VHB tape and copper electrode (1 × 3 cm^2). The DI water dried at 60 ^oC for 5 h.

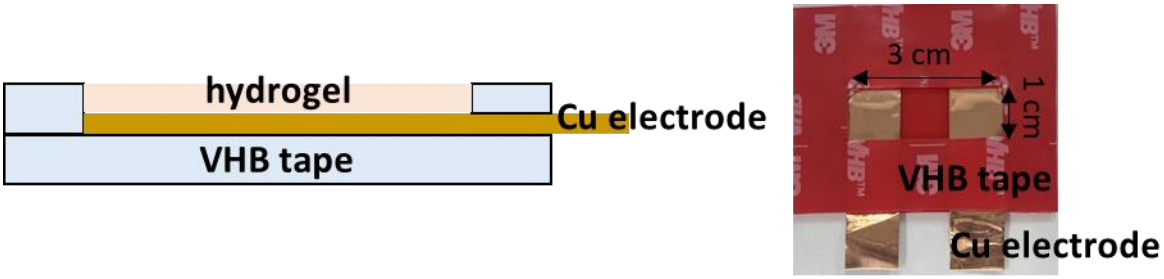

Wearable TGC.

Copper tapes were stacked on the VHB tape (2 × 5 cm^2). The VHB tape with (2 × 3 cm^2) hole was stacked on the VHB tape and Copper electrodes. The solution was drop cast on the VHB tape and copper electrode (2 × 3 cm^2). The DI water dried at 60 ^oC for 5 h. Two TGCs were attached each other.

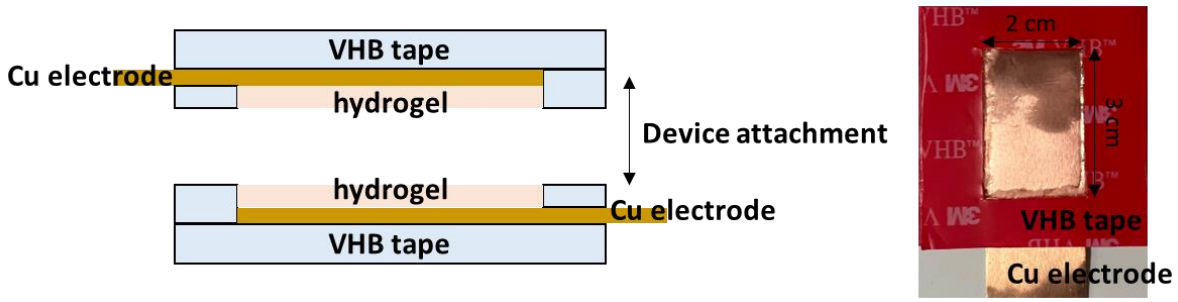

Sandwich structured TGC.

Silver paste as the electrode was stacked on bare glass (1 × 5 cm^2). The glass was annealed on the 50 ^oC hot plate for 2 h. The VHB 4905 with hole (a diameter of 0.6 cm and thickness of 0.5 cm) was stacked on the silver paste electrodes. The solution was drop cast on the silver paste electrode (a diameter of 0.6 cm and thickness of 0.5 cm). The DI water dried at 60 ^oC for 5 h. The process was repeated until the polymer gel reached a height of 0.5 cm. The sandwich-structured TGC had a cross-sectional area of 0.09 × π cm^2 and an effective length between the electrodes of 0.5 cm.

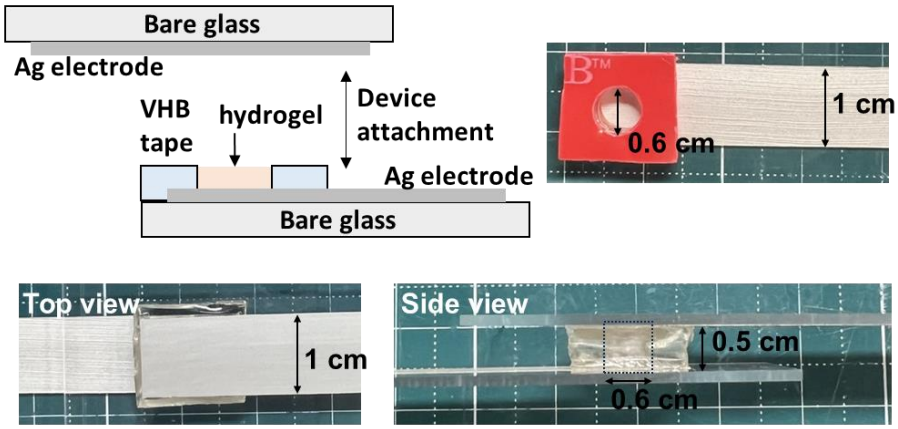

Application using the wearable TGC (LED working).

Yellow LED worked when over 1.7 V was applied at 100.5 μA. To light up the LED, wearable TGC was aided by a voltage amplifier (AD620), which it increased the voltage to 2 V.

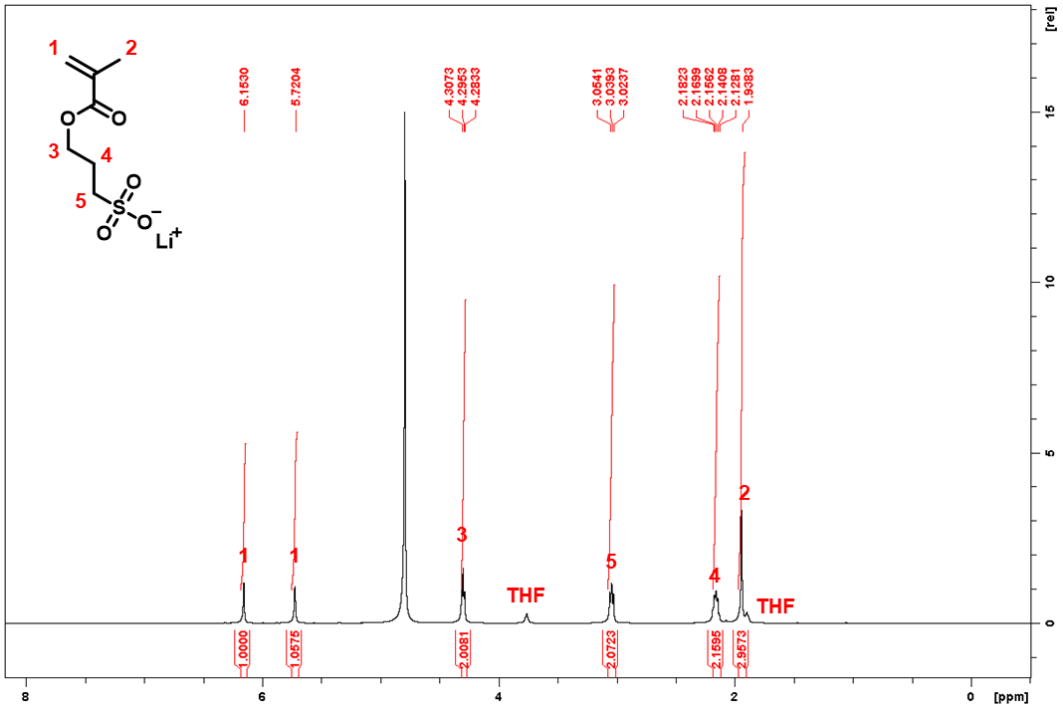

^{1}H NMR spectroscopy of lithium sulfopropyl methacrylate (Li[SPMA]).

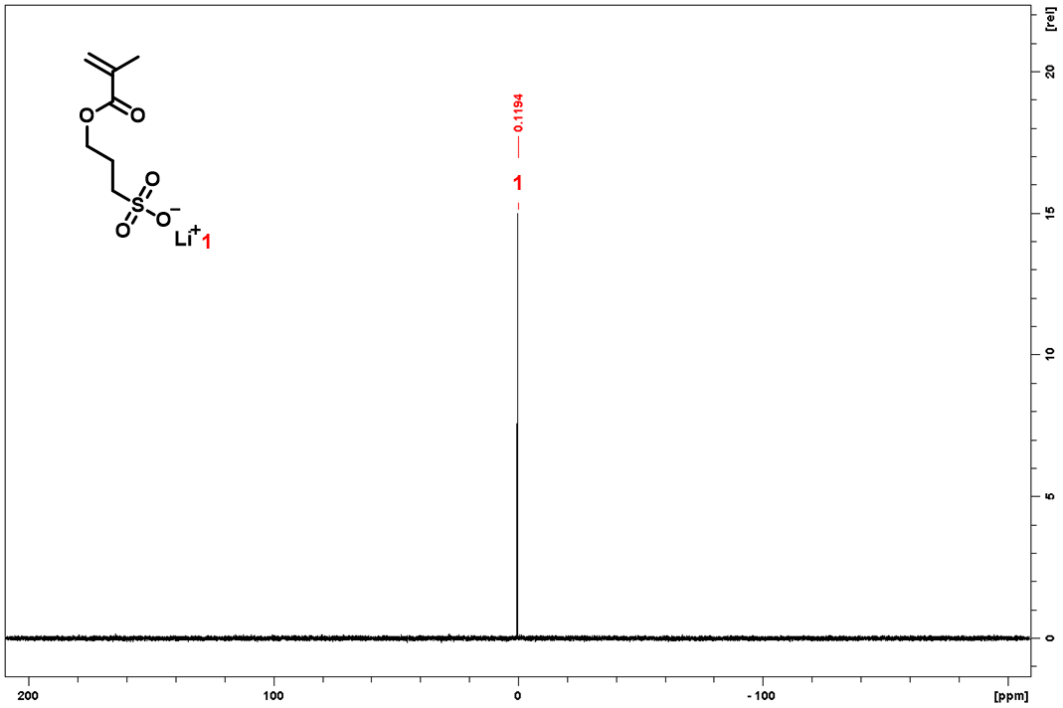

^{7}Li NMR spectroscopy of lithium sulfopropyl methacrylate (Li[SPMA]).

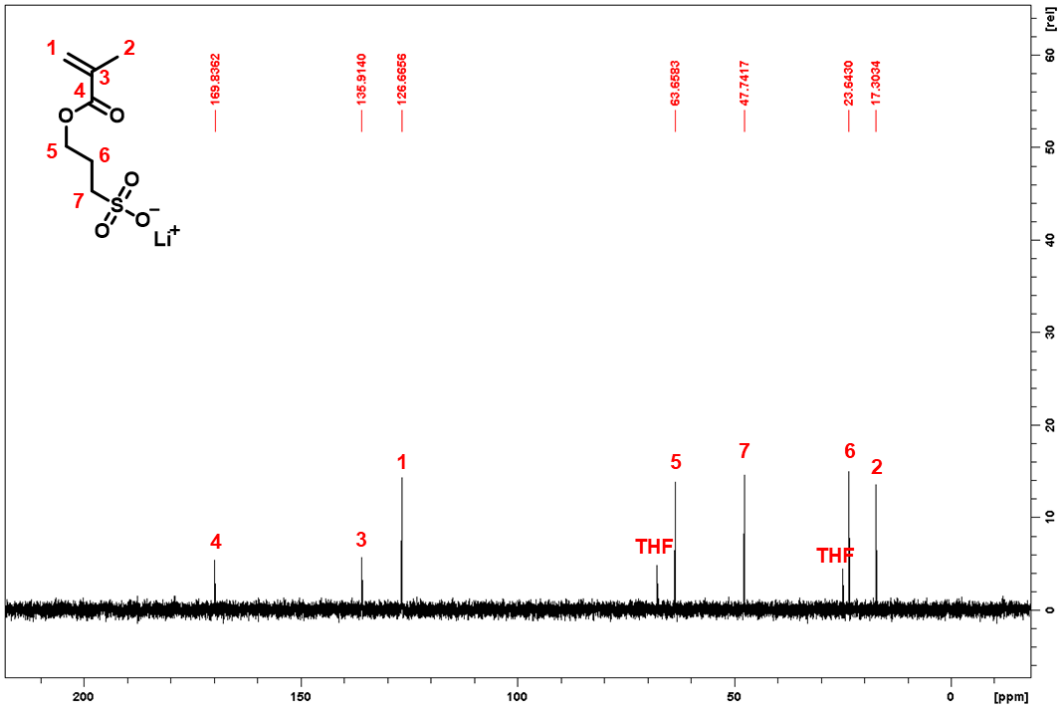

^{13}C NMR spectroscopy of lithium sulfopropyl methacrylate (Li[SPMA]).

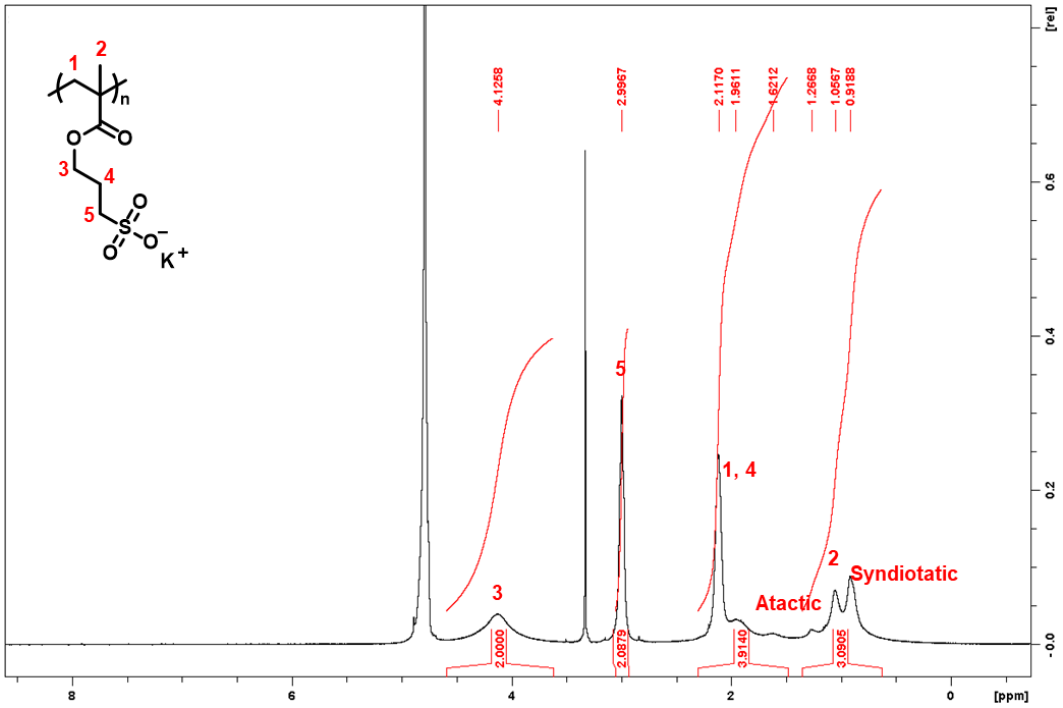

^{1}H NMR spectroscopy of PKSP.

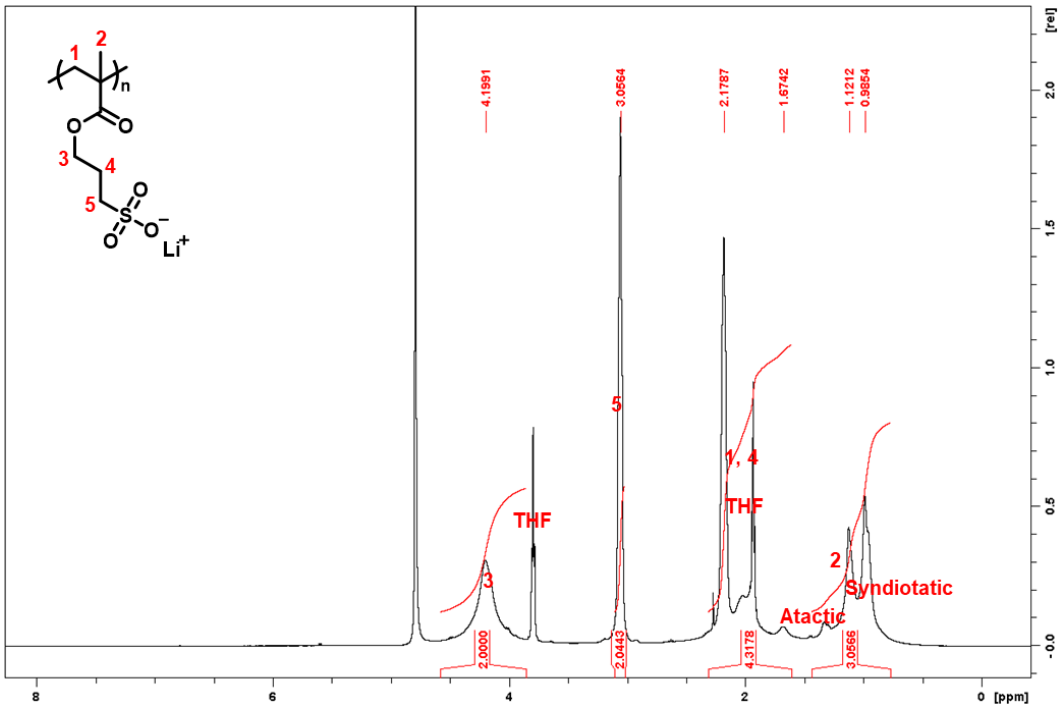

^{1}H NMR spectroscopy of PLSP.

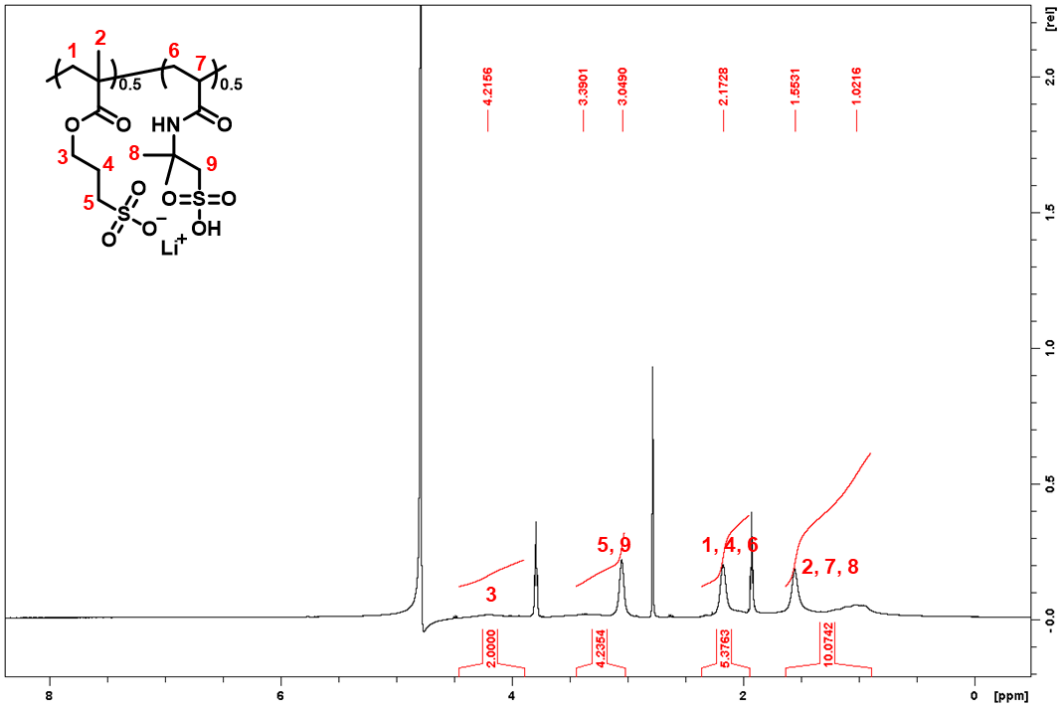

^{1}H NMR spectroscopy of PLAM.

Figure S1. The ^{1}H NMR, ^{7}Li NMR, and ^{13}C NMR spectra of lithium sulfopropyl-methacrylate (Li[SPMA]) and ^{1}H NMR spectra of PKSP, PLSP, and PLAM.

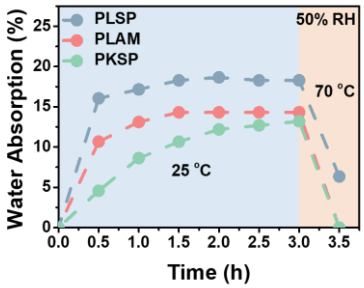

Figure S2. The water absorption of the PKSP, PLSP, and PLAM depending on the exposure time to 50% RH at 25 °C, and the water evaporation over time at 70 °C.

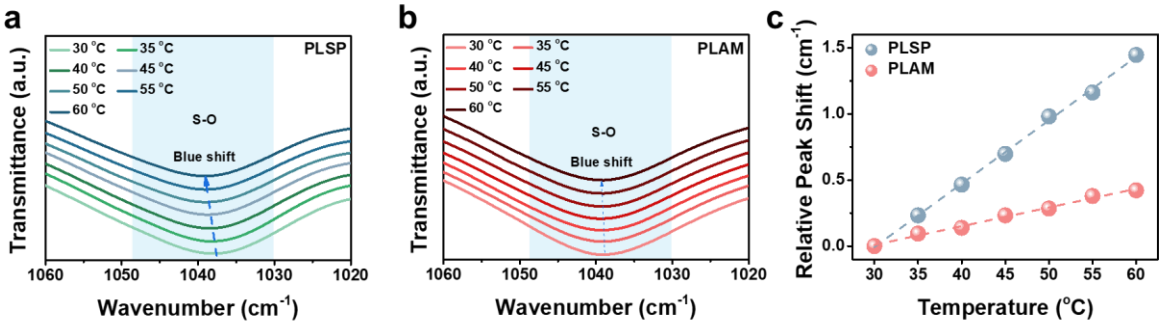

Figure S3. The FT-IR spectra of the a) PLSP, b) PLAM, and c) relative peak shift of the anionic polymers depending on the temperature (30 ~ 60 °C).

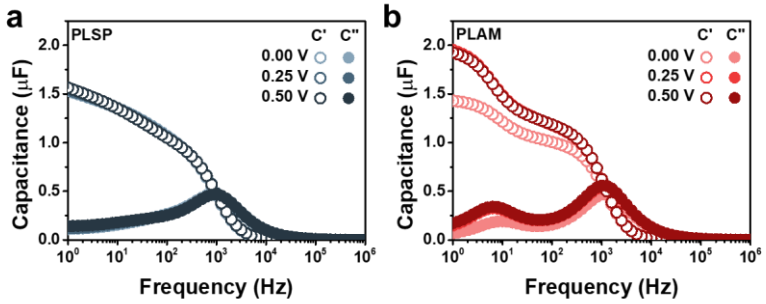

Figure S4. The real and imaginary capacitance of the a) PLSP and b) PLAM at frequencies 10^0 and 10^6 Hz at DC voltage of 0, 0.25, 0.50 V.

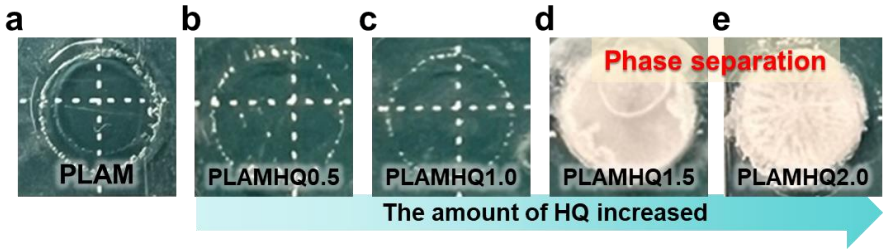

Figure S5. Photographic images of the PLAM films with various amounts of HQ: a) 0% (PLAM), b) 0.5% (PLAMHQ0.5), c) 1.0% (PLAMHQ1.0), d) 1.5% (PLAMHQ1.5), and e) 2.0% (PLAMHQ2.0).

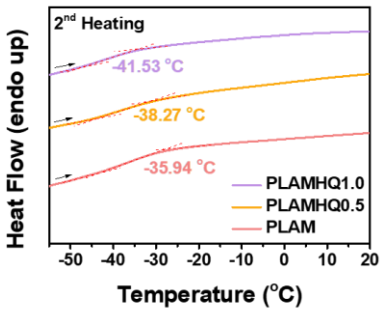

Figure S6. The phase changes in the various PLAM-based films during differential scanning calorimetry (DSC).

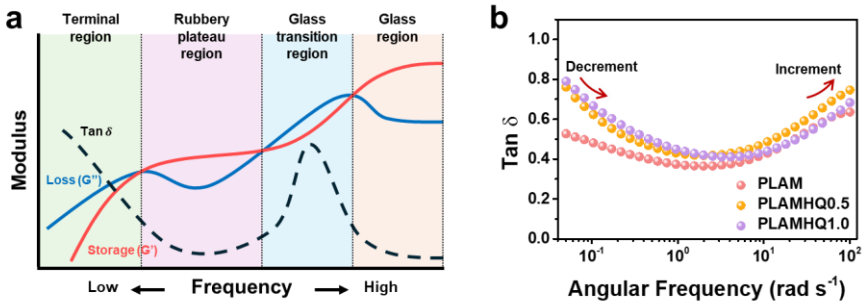

Figure S7. a) Diagram of the polymer modulus (G', G", and Tan δ) depending on the frequency. b) The tan δ of of the PLAM, PLAMHQ0.5, and PLAMHQ1.0 under angular frequency.

Polymer behavior is categorized into 4 regions: terminal, rubbery plateau, glass transition, and glass region (**Fig. S7a**). The rubbery plateau and the glass region are the only regions where the storage moduli above the loss moduli in 4 regions. However, after the glass region, there is no longer a region where the loss moduli is above storage moduli, resulting in a continuous decrease of tan δ. On the contrary, there are terminal and glass transition regions before and after the rubbery plateau region. Within these regions, the loss moduli surpass the storage moduli. Consequently, the tan δ exhibits to decrease and subsequently increase from low frequency to high frequency. The polymer samples exhibited similar behavior, therefore demonstrating that they were in a rubbery plateau region (**Fig. S7b**).

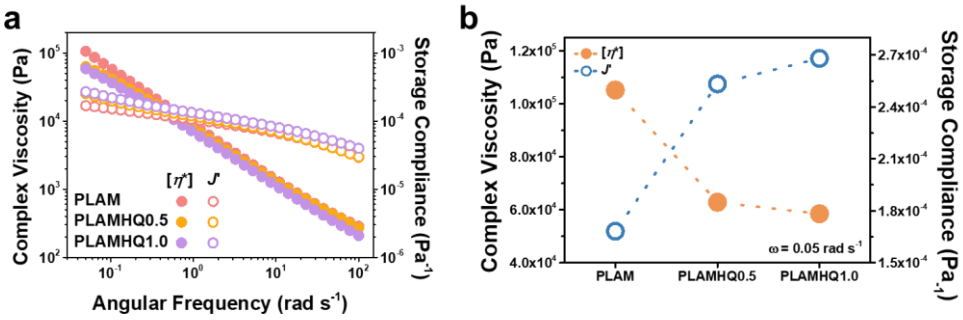

Figure S8. Complex viscosity and storage compliance of the PLAM, PLAMHQ0.5, and PLAMHQ1.0 a) under angular frequency and b) under 0.05 rad s^{-1}.

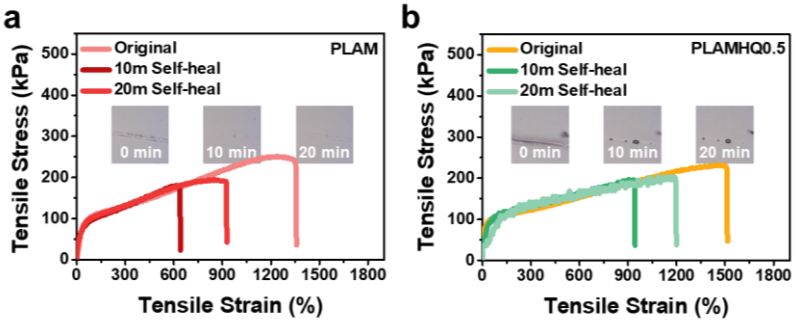

Figure S9. The tensile stress-strain (S-S) curve of a) the PLAM and b) the PLAMHQ0.5, along with inset visual images of the PLAM and PLAMHQ0.5.

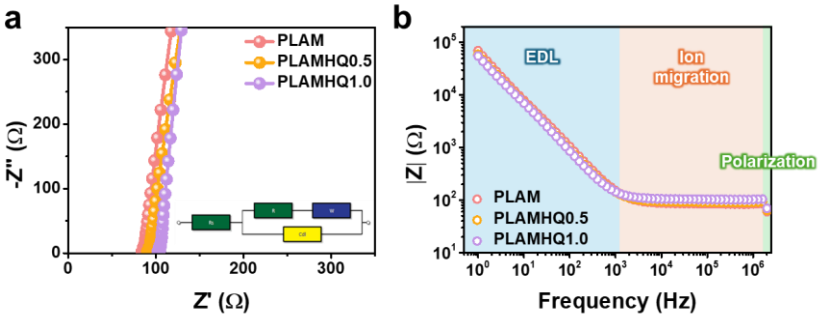

	Resistance (Ω)	Ionic Conductivity (mS cm^{-1})
PLAM	84.87	1.25
PLAMHQ0.5	91.44	1.16
PLAMHQ1.0	103.37	1.03

Figure S10. The a) Nyquist plots, along with an inset showing an equivalent circuit model, and b) Bode plots of the various PLAM-based films: PLAM, PLAMHQ0.5, and PLAMHQ1.0. (R_s : bulk resistance, R : charge transfer resistance, W: Warburg elements, and C_{dl} : capacitance of the electrochemical double-layer)

Impedance ($Z(w)$) is classified into 3 regions: polarization, ion migration, and EDL. In the polarization region (10^6 Hz ~), a decrement in frequency leads to an increment in ion organization, resulting in a rise in capacitance. Consequently, $Z(w)$ increases. However, in the ion migration region (10^3 ~ 10^6 Hz), there is no increase in capacitance, and resistance is also consistent. Therefore, a constant $Z(w)$ was observed. In the EDL region (~ 10^3 Hz), as ions accumulate at the electrode interface, capacitance increases, and $Z(w)$ increases.[S3] The ion conductivity was determined from the impedance in the ion migration region.

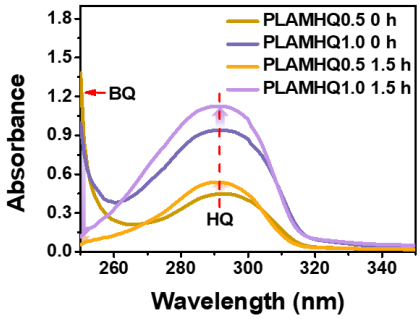

Figure S11. The time-dependent UV-vis spectra of the PLAMHQ0.5 and the PLAMQH1.0.

The ratio between HQ and BQ is quantitatively confirmed via the Beer-Lambert Law ($A = \varepsilon lc$), where A, ε, l, and c are the absorbance, absorptivity, optical path length, and concentration, respectively. Since absorbance is obtained from the same sample, assuming that absorptivity and optical path length are the same, the absorbance ratio is equal to the ratio of the two species. Thus, the concentration ratio of HQ to BQ (i.e., [HQ]/[BQ]) was determined by evaluating the absorbances at the corresponding maximum absorption wavelengths of 292 nm and 250 nm. Thus, the PLAMHQ0.5 and PLAMHQ1.0 exhibited [HQ]/[BQ] of 9.26 and 9.59, respectively.

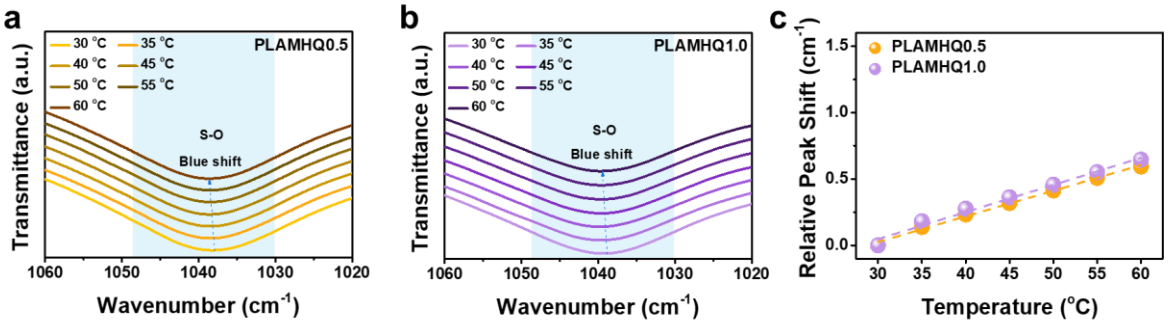

Figure S12. The FT-IR spectra of the a) PLANHQ0.5, b) PLAMHQ1.0, and c) relative peak shift of the anionic polymers depending on the temperature (30 ~ 60 °C).

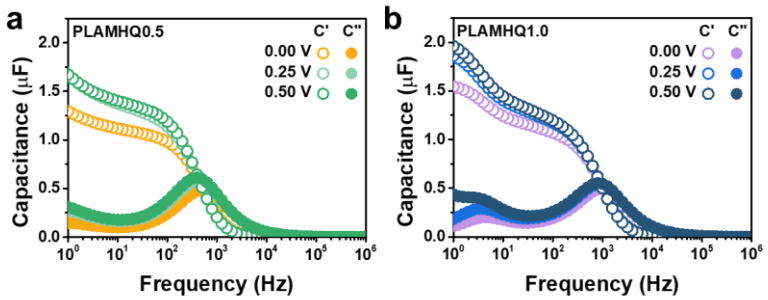

Figure S13. The real and imaginary capacitance of the a) PLAMHQ0.5 and b) PLAMHQ1.0 at frequencies 10^0 and 10^6 Hz at DC voltage of 0, 0.25, 0.50 V.

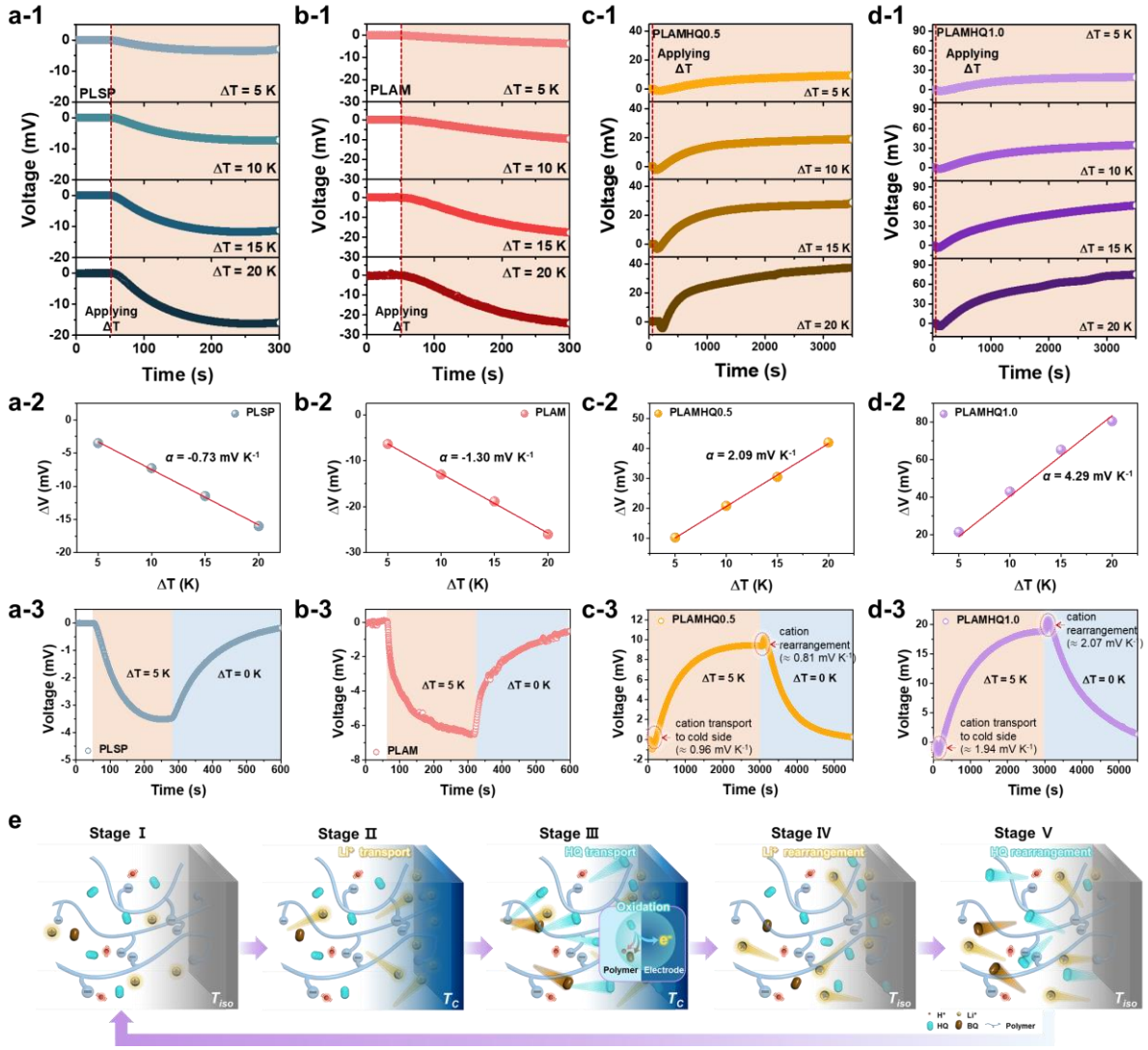

Figure S14. The ΔV *vs.* time profiles of the a-1, 2, 3) PLSP, b-1, 2, 3) PLAM, c-1, 2, 3) PLAMHQ0.5, and d-1, 2, 3) PLAMHQ1.0 depending on the temperature difference (ΔT) and after removing the temperature gradient. e) The working mechanism of TGCs based on PLAMHQ on the cold side.

Ⅰ. Random distribution of mobile materials under isothermal state (T_{iso}).

Ⅱ. Immediately after the temperature gradient was formed, the rapid transport of Li^+ from the hot side to the cold side. Generation of negative thermal-volage resulting from the EDL by Li^+.

Ⅲ. Dominant HQ in the pH-controllable PLAM was transported from the hot side to the cold side, leading to the positive thermal-voltage by the oxidation reaction.

Ⅳ. Immediately after the temperature gradient vanished, there was a rapid rearrangement of Li^+. Consequently, as the Li^+ rearranged, positive thermal-voltage rapidly increased.

Ⅴ. Subsequently, the thermal-voltage diminished as a result of the rearrangement of HQ and eventually returned to its initial state.

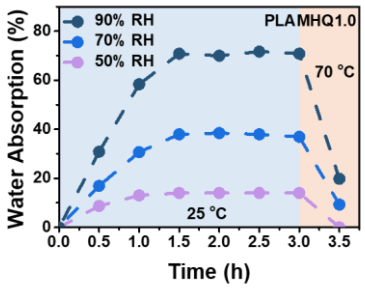

Figure S15. The water absorption of the PLAMHQ1.0 depending on the exposure time to various RH conditions (50%, 70%, and 90% RH), and the water evaporation over time at 70 °C.

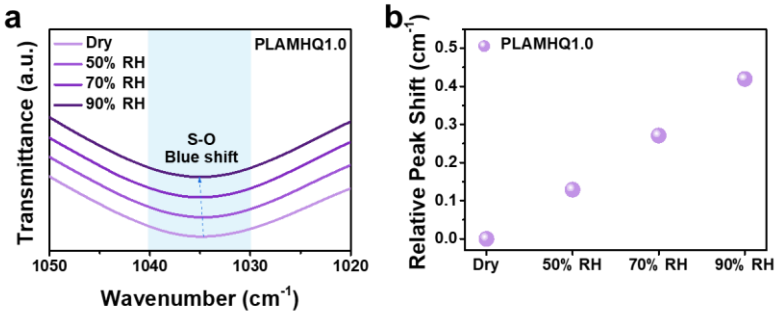

Figure S16. The FT-IR spectra of the a) PLAMHQ1.0, and b) relative peak shift depending on the various RH (dry, 50%, 70%, and 90% RH).

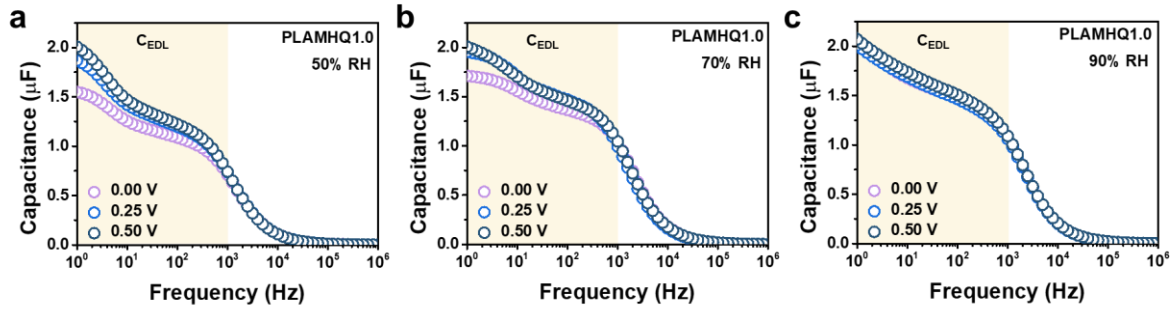

Figure S17. The complex capacitance of the PLAMHQ1.0 under a) 50% RH, b) 70% RH, and c) 90% RH at frequencies 10^0 and 10^6 Hz at DC voltages of 0, 0.25, and 0.50 V.

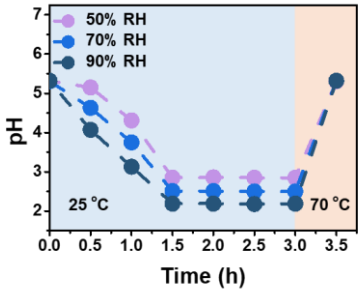

Figure S18. a) The observed changes in pH according to the water retention in the polymer matrix at various RH conditions (50%, 70%, and 90% RH) and 70 ^{o}C.

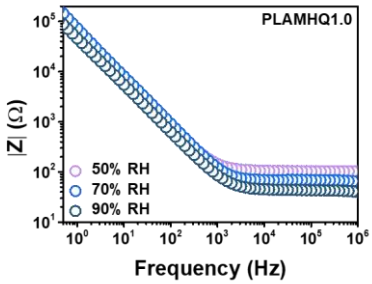

RH condition (%)	Resistance (Ω)	Ionic Conductivity (mS cm^{-1})
50	103.37	1.03
70	69.00	1.54
90	43.32	2.46

Figure S19. Bode plots of PLAMHQ1.0 at various RH conditions (50%, 70%, and 90% RH).

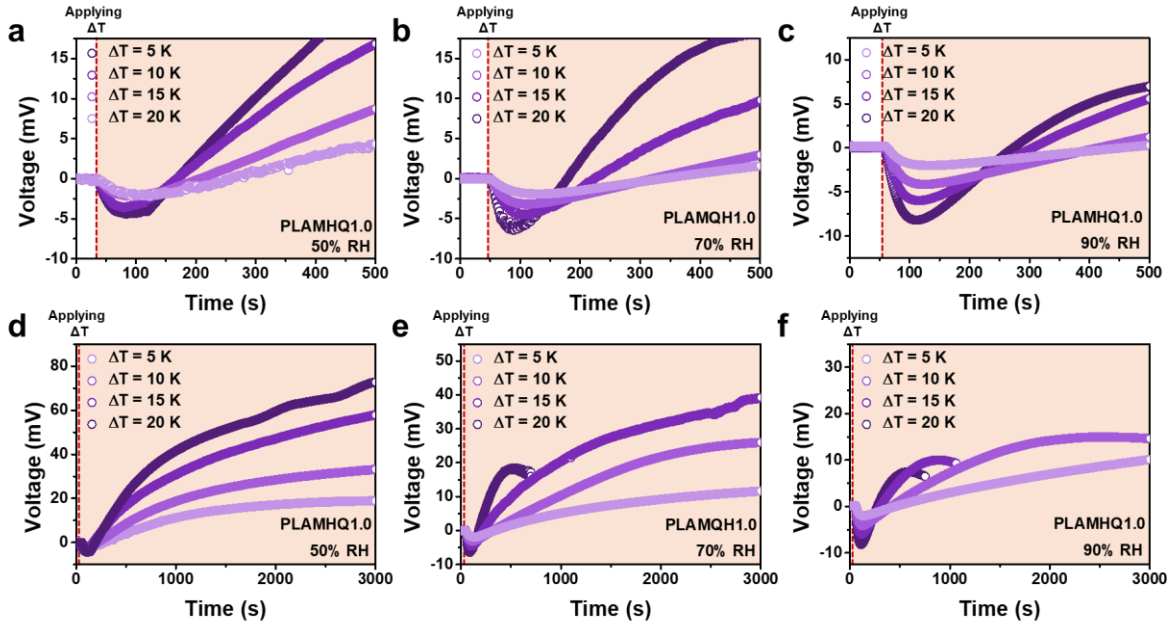

Figure S20. The initial ΔV *vs.* time profiles of PLAMHQ1.0 at a) 50% RH, b) 70% RH, and c) 90% RH. The ΔV *vs.* time profiles of PLAMHQ1.0 at d) 50% RH, e) 70% RH, and f) 90% RH.

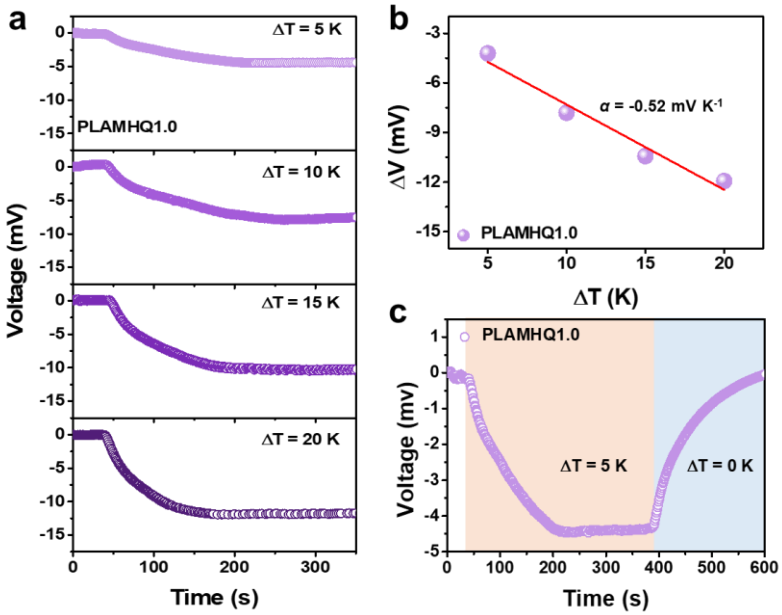

Figure S21. a, b, and c) The ΔV *vs.* time profiles of the completely dried PLAMHQ1.0 depending on the temperature difference (ΔT) and after removing the temperature gradient.

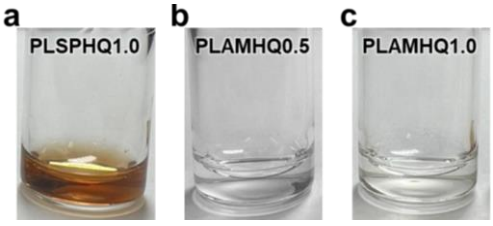

Figure S22. Photographic images showing the solution color of a) the PLSPHQ1.0, b) the PLAMHQ0.5, and c) the PLAMHQ1.0.

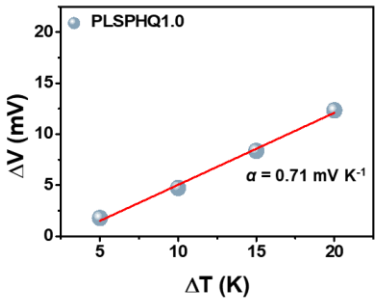

Figure S23. The ΔV *vs.* ΔT plots of the PLSPHQ1.0.

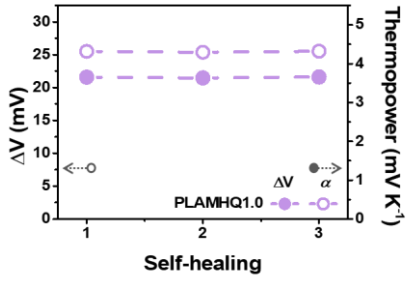

Figure S24. The voltage and thermopower of the PLAMHQ1.0 at ΔT = 5 K after various amounts of self-healing time.

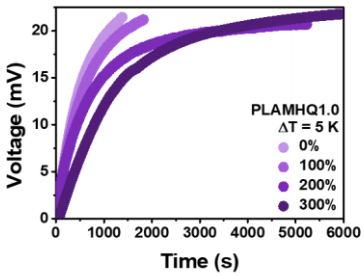

Figure S25. The voltage *vs*. time profiles of the PLAMHQ1.0 under 0, 100, 200, and 300% uniaxial stretching at ΔT = 5 K.

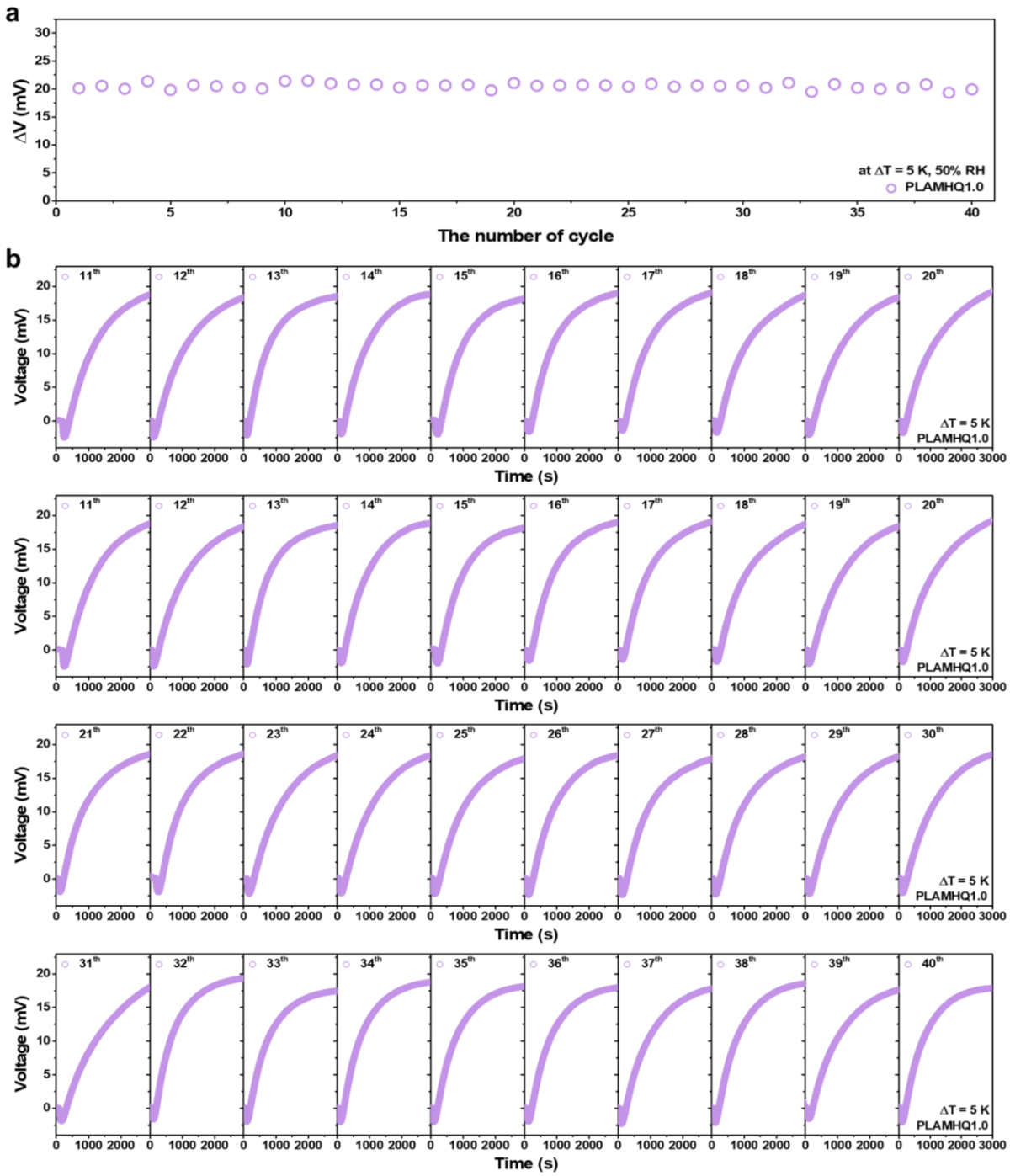

Figure S26. a) voltage depending on the number of cycles and b) ΔV *vs.* time profiles at ΔT = 5 K.

Table S1. Performance calculation values for each performance of PLAMHQ0.5 and PLAMHQ1.0.

	T_H (K)	V_{oc} (mV)	I (μA)	J_{sc} (A m^{-2})	P_{max} (mW m^{-2})	$P_{max}/\Delta T^2$ (μW m^{-2} K^{-2})	η (%)	η_r (%)
PLAMHQ0.5	303	10.28	7.83	0.28	0.78	31.33	0.0060	0.37
	308	20.82	12.20	0.43	2.62	26.18	0.010	0.31
	313	30.49	19.01	0.97	5.63	25.04	0.014	0.30
	318	41.95	24.75	0.88	10.70	26.76	0.021	0.33
PLAMHQ1.0	303	21.41	12.02	0.43	2.27	90.73	0.016	0.98
	308	42.92	24.90	0.88	9.44	74.44	0.034	1.04
	313	65.28	36.69	1.30	21.23	94.38	0.051	1.05
	318	80.44	46.30	1.64	32.94	82.34	0.059	0.94

Table S2. A comparison of the TGC performance, thermopower, Carnot relative efficiency, stretchability, and self-healing capability of previously-reported TGC devices.

Polymer	Redox couples	Type	State	α (mV K^{-1})	η_r (%)	Stretchability (%)	Self-healing	Ref
-	I_3^-/I^-	n	liquid	2	0.003	-	-	[S4]
-	$Co(bpy)3^{2+}/Co(bpy)3^{3+}$	n	liquid	1.6	0.087	-	-	[S5]
-	Fe^{2+}/Fe^{3+}	n	liquid	1.74	0.45	-	-	[S6]
-	Fe^{2+}/Fe^{3+}	n	liquid	1.66	0.23	-	-	[S6]
-	Fe^{2+}/Fe^{3+}	n	liquid	1.04	0.11	-	-	[S6]
-	Fe^{2+}/Fe^{3+}	n	liquid	0.37	0.005	-	-	[S6]
-	Li^+/Li	n	liquid	2.10	0.32	-	-	[S7]
-	Li^+/Li	n	liquid	1.85	0.43	-	-	[S8]
-	Cu^{2+}/Cu	n	liquid	0.84	0.091	-	-	[S9]
-	Cu^{2+}/Cu	n	liquid	1.09	0.033	-	-	[S10]
-	Fe^{2+}/Fe^{3+}	n	liquid	1.63	0.24	-	-	[S10]
PLAMHQ1.0	Hydroquinone	n	gel	4.29	1.05	1703	20 min at r.t	This work

a) poly(acrylamide), b) poly(acrylamide-co-2-acrylamido-2-methyl-1-propane sulfonic acid).

Reference

1. J. H. Kwon, Y. M. Kim and H. C. Moon, *ACS Nano*, 2021, **15**, 9, 15132.
2. O. Larsson, E. Said, M.Berggren and X. Crispin, *Adv. Funct. Mater.*, 2009, **19**, 3334.
3. J. Jeong, G. C. Marques, X. Feng, D. Boll, S. A. Singaraju, J. Aghassi-Hagmann, H. Hahn and B. Breitung, *Adv. Mater. Interfaces*, 2019, **6**, 1901074.
4. H. Zhou, T. Yamada and N. Kimizuka, *J. Am. Chem. Soc.*, 2016, **138**, 10502.
5. P. F. Salazar, S. T. Stephens, A. H. Kazim, J. M. Pringle and B. A. Cola, *J. Mater. Chem. A*, 2014, **2**, 20676.
6. K. Kim, S. Hwang and H. Lee, *Electrochim. Acta*, 2020, **335**, 135651.
7. K. Kim and H. Lee, *Phys. Chem. Chem. Phys.*, 2018, **20**, 23433.
8. K. Kim and H. Lee, *Energy Technol*. 2019, **7**, 1900857.
9. A. Gunawan, C. -H. Lin, D. A. Buttry, V. Mujica, R. A. Taylor, R. S. Prasher and P. E. Phelan, *Nanoscale Microscale Thermophys. Eng.*, 2013, **17**, 304.
10. U. B. Holeschovsky, *Analysis of flooded flow fuel cells and thermogalvanic generators*. Massachusetts Institute of Technology,1994.